UC Berkeley
UC Berkeley Previously Published Works

Title
The Influence of Atmospheric River Seasonality and Orientation on Pacific Northwest Surface Temperatures

Permalink
https://escholarship.org/uc/item/9401p78m

Journal
Journal of Geophysical Research: Atmospheres, 131(16)

ISSN
2169-897X

Authors
Goddard, PB
O'Brien, TA
Zhou, Y
et al.

Publication Date
2026-08-28

DOI
10.1029/2026jd046646

Copyright Information
This work is made available under the terms of a Creative Commons Attribution License, available at https://creativecommons.org/licenses/by/4.0/

Peer reviewed

eScholarship.org Powered by the California Digital Library
University of California

Check for updates

JGR Atmospheres

RESEARCH ARTICLE
10.1029/2026JD046646

The Influence of Atmospheric River Seasonality and Orientation on Pacific Northwest Surface Temperatures

P. B. Goddard[1], T. A. O'Brien[1,2], Y. Zhou[2], and W. D. Collins[3]

[1]Earth and Atmospheric Sciences, Indiana University, Bloomington, IN, USA, [2]Earth and Environmental Sciences, Lawrence Berkeley National Laboratory, Berkeley, CA, USA, [3]School of Environmental Sciences, University of East Anglia, Norwich, UK

Key Points:

- Winter atmospheric rivers (ARs) tend to be meridionally aligned and are associated with persistent regional warming
- Summer ARs show weak composite temperature signals because different AR orientations produce opposing temperature responses that cancel
- The offshore orientation of an approaching AR provides advance predictability of downstream temperature anomalies

Supporting Information:

Supporting Information may be found in the online version of this article.

Correspondence to:

P. B. Goddard,
pgoddard@iu.edu

Citation:

Goddard, P. B., O'Brien, T. A., Zhou, Y., & Collins, W. D. (2026). The influence of atmospheric river seasonality and orientation on Pacific Northwest surface temperatures. *Journal of Geophysical Research: Atmospheres*, *131*, e2026JD046646. https://doi.org/10.1029/2026JD046646

Received 10 FEB 2026
Accepted 5 AUG 2026

Author Contributions:

Conceptualization: P. B. Goddard, T. A. O'Brien, W. D. Collins
Data curation: P. B. Goddard
Formal analysis: P. B. Goddard
Funding acquisition: T. A. O'Brien, W. D. Collins
Methodology: P. B. Goddard, T. A. O'Brien
Project administration: T. A. O'Brien
Software: T. A. O'Brien, Y. Zhou
Visualization: P. B. Goddard
Writing – original draft: P. B. Goddard

© 2026 The Author(s). Journal of Geophysical Research: Atmospheres published by Wiley Periodicals LLC on behalf of American Geophysical Union. This is an open access article under the terms of the Creative Commons Attribution License, which permits use, distribution and reproduction in any medium, provided the original work is properly cited.

Abstract Atmospheric rivers (ARs) influence weather and climate along the North American west coast, yet their effects on Pacific Northwest (PNW) surface temperatures remain unclear across seasons and synoptic configurations. Motivated by the 2021 PNW heatwave—which was preceded by a poleward-tracking AR—we analyze how ARs modulate daily maximum temperatures (T_{max}) during summer (JJA) and winter (DJF) from 1989 to 2024. Using reanalysis data and an AR detection algorithm, we composite integrated vapor transport (IVT), Z500, total precipitation, cloud cover, and T_{max} anomalies for AR detection days and the subsequent 10 days, and classify summer ARs according to the tilt of their IVT plumes as meridionally oriented (MARs) or zonally oriented (ZARs). Winter ARs exhibit a coherent southwest to northeast orientation and generate widespread, statistically significant PNW warming that persists for over a week. In contrast, composite summer ARs produce no consistent T_{max} response due to the cancellation of ARs that track north versus south of the region. Separating JJA ARs by orientation reveals a strong dynamical divide: MARs induce substantial warming (>3°C in the median T_{max}), associated with a northeast-tilted ridge that enhances subsidence and poleward heat transport, whereas ZARs generate significant cooling tied to zonal flow and inland advection of cool, moist marine air. These results show that AR seasonality and orientation jointly influence the sign and magnitude of PNW temperature anomalies. Importantly, AR orientation at a fixed offshore detection region provides predictive value for downstream thermal impacts beyond AR intensity and ridge strength, improving heat-extreme forecasting in a warming climate.

Plain Language Summary Atmospheric rivers—long, narrow bands of moisture that often bring heavy rain to the North American west coast—can also strongly affect temperatures in the Pacific Northwest (PNW), but their impact depends on both the season and the direction they take. Using more than 30 years of weather data, this study finds that winter atmospheric rivers consistently warm the region, as they typically transport warm air northward and produce elevated temperatures that can last for over a week. In summer, atmospheric rivers do not show a clear temperature effect unless they are separated by orientation: storms that tilt northward tend to cause substantial warming, while those moving more directly from west to east often cool the region by drawing in marine air. This distinction helps explain why an atmospheric river contributed to warming ahead of the 2021 PNW heatwave, while also showing that atmospheric rivers alone cannot account for such extreme events. Importantly, the results demonstrate that the orientation of an approaching atmospheric river offshore provides useful advance information about whether temperatures in the PNW are likely to rise or fall, offering potential benefits for forecasting heat extremes in a warming climate.

1. Introduction

In late June to early July 2021, an extreme heatwave devastated the North American Pacific Northwest (PNW), bringing unprecedented temperatures. Temperature anomalies exceeded previous records by more than 3°C and reached up to 6°C above previous records in some areas, spanning from Portland, Oregon, to British Columbia, Canada. This event resulted in the loss of hundreds of human lives and severe disruptions to local ecosystems (Overland, 2021; Philip et al., 2022; White et al., 2023). Event attribution analyses indicate that anthropogenic warming increased the intensity of the 2021 PNW heatwave by roughly 1°–2°C relative to preindustrial conditions (Bercos-Hickey et al., 2022; Fleishman et al., 2025; Philip et al., 2022; Terray, 2023). Complementary analyses indicate that the event was exceedingly rare in the historical climate, with estimates ranging from one in hundreds to thousands of years depending on method and framing (Fleishman et al., 2025; Heeter et al., 2023;

Writing – review & editing:
P. B. Goddard, T. A. O'Brien, Y. Zhou, W. D. Collins

McKinnon & Simpson, 2022; Philip et al., 2022). Furthermore, similar events could see temperature anomalies rise by as much as 5°C by the end of the 21st century (Bercos-Hickey et al., 2022).

The PNW heatwave was an extraordinary compound weather event driven by both dynamic and thermodynamic processes. Dynamically, an upstream cyclone released latent heat, intensifying a blocking anticyclone over the region two to 3 days before the onset of extreme temperatures (Neal et al., 2022). The ridge has been linked to anomalous convection in the Southeast Asian summer monsoon, which triggered a trans-Pacific Rossby wave train (Lin et al., 2022; Qian et al., 2022). This cyclone and anticyclone wave train developed into an "Omega Block" contributing to the development of a heat dome in the region characterized by adiabatic warming through air subsidence (Zhang et al., 2023). Additionally, these atmospheric dynamics facilitated the arrival of a warm-season North Pacific atmospheric river, which transported moisture and heat energy into the region in the days leading up to the heatwave, further reinforcing the high-pressure system (Mo et al., 2022).

Thermodynamic and land-surface processes, particularly soil desiccation and associated land-atmosphere feedbacks (Duan et al., 2025), also played a crucial role in the extreme heatwave. In the weeks leading up to the event, a quasi-resonant amplification of a planetary wave established a persistent high-pressure system near the PNW, driving advection of dry hot air into the region resulting in significant local soil moisture deficits (Li et al., 2024). These deficits limited evaporative cooling, allowing more energy to be converted into sensible heat, thereby intensifying atmospheric warming (Miralles et al., 2014; Schumacher et al., 2022). This positive feedback mechanism contributed to a nonlinear temperature response, surpassing what would be expected from linear climate warming trends alone (Bartusek et al., 2022; McKinnon & Simpson, 2022). The influence of land-atmosphere feedbacks on extreme heatwaves is expected to intensify as drought conditions become more frequent over the 21st century (Domeisen et al., 2022).

While these studies have established the key dynamic and thermodynamic mechanisms responsible for the 2021 PNW heatwave, less attention has been given to how recurring synoptic patterns—particularly atmospheric rivers (ARs)—modulate regional temperature extremes under varying seasonal and geometric configurations. The 2021 event, in which a North Pacific AR preceded the heatwave peak by roughly a week, highlights the potential role of AR-related moisture and heat transport in shaping PNW temperature anomalies (Mo et al., 2022). Notably, the analysis by Mo et al. (2022) suggests that sensible heat flux convergence associated with the atmospheric river over southwestern Canada played an important role in the northward expansion of the heatwave from the south. This result is supported by the work of Scholz and Lora (2024) who demonstrate that ARs substantially warm the regions where they make landfall by advecting large amounts of sensible and latent heat from lower latitudes. As these moisture-laden air masses ascend coastal topography or encounter blocking highs, the resulting convergence of warm, humid air enhances downward longwave radiation and surface sensible heat fluxes, leading to strong near-surface warming. Their analysis shows that ARs are associated with widespread positive temperature anomalies—often exceeding +5°C—across the mid-latitudes and that more than two-thirds of extreme warm anomalies coincide with AR occurrences.

To assess this relationship between ARs and surface temperature anomalies systematically, we examine how ARs that approach the PNW affect temperature anomalies during boreal summer (JJA) and winter (DJF). Motivated by the JJA results, we hypothesize that ARs with a stronger south-to-north tilt may preferentially transport warmer air from lower latitudes, leading to enhanced warm anomalies in the PNW. Accordingly, we distinguish between meridionally tilted and zonally oriented ARs to evaluate how their geometry shapes regional temperature responses. By contrasting AR-associated circulation and temperature anomalies across seasons and AR geometries, we aim to clarify the dynamical regimes that enhance or suppress PNW warming and identify whether the processes that preconditioned the 2021 heatwave are representative of broader climatological behavior.

2. Methods

2.1. Atmospheric River Detection

We identify ARs using the Toolkit for Extreme Climate Analysis Bayesian AR Detector (TECA-BARD; O'Brien et al., 2020) applied to the ERA5 reanalysis dataset (Hersbach et al., 2020) for the period December 1989–August 2024, focusing on the DJF and JJA seasons. ERA5 provides hourly data at a spatial resolution of $0.25° \times 0.25°$ in latitude and longitude. TECA-BARD assigns probabilities that a given integrated vapor transport (IVT) field—defined as the vertical integral of horizontal water vapor flux (e.g., kg m^{-1} s^{-1})—represents an AR, based

21698996, 2026, 16, Downloaded from https://agupubs.onlinelibrary.wiley.com/doi/10.1029/2026JD046646, Wiley Online Library on [11/11/2026]. See the Terms and Conditions (https://onlinelibrary.wiley.com/terms-and-conditions) on Wiley Online Library for rules of use; OA articles are governed by the applicable Creative Commons License

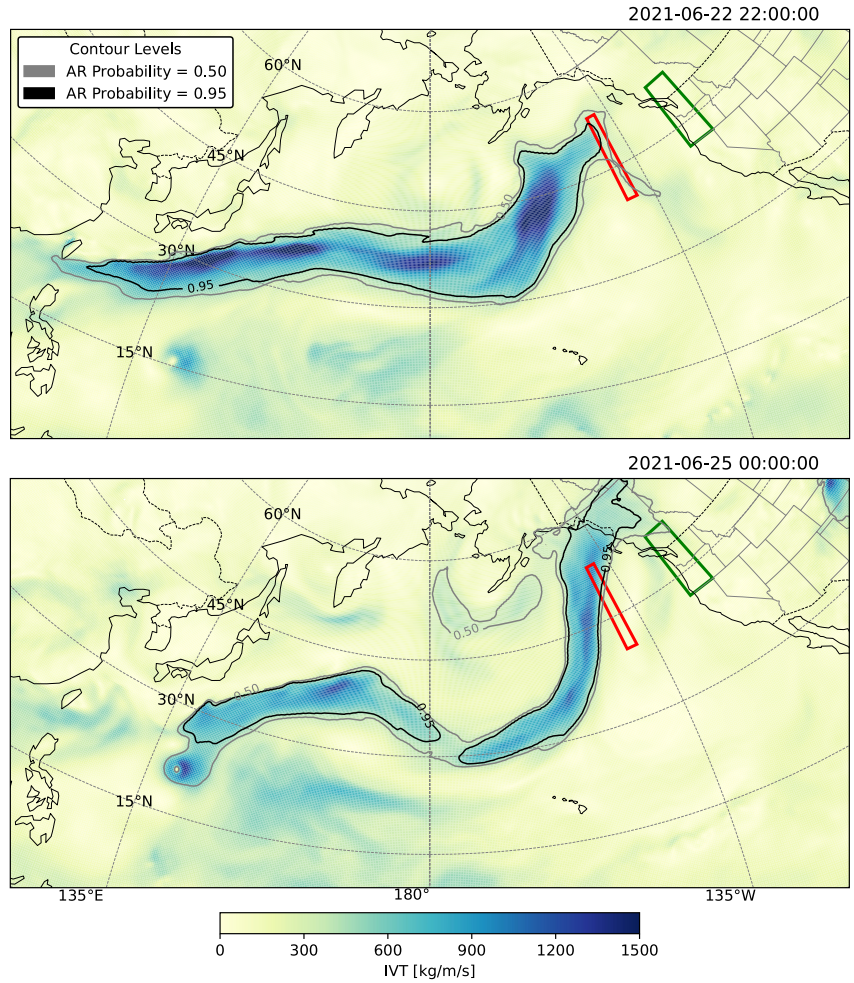


Figure 1. Integrated vapor transport with atmospheric river (AR) probability contours coinciding with the AR event that made landfall prior to the June–July 2021 Pacific Northwest (PNW) heatwave event. For Results Section 3.1 of this study, we identify the dates when an AR (probability ≥ 0.95) first enters the detection region (red box) and track the subsequent 10 days provided that no AR is present within the PNW region (green box) during those days. Therefore, the upper panel would represent an AR detection day, 2021-06-22, and the lower panel would represent AR Day +3. See Methods Section 2.1 for further details.

on its magnitude, spatial extent, and geographic location. In this study, grid cells with an AR probability exceeding 95% are classified as AR occurrences.

We identify and record the dates when an AR first enters the detection region in the Northeast Pacific (140°–138°W, 40°–53°N; red box in Figure 1). This offshore region is selected to capture ARs prior to landfall along the west coast of North America, thereby preserving their large-scale structure and orientation before modification by land–atmosphere and orographic interactions. The latitudinal extent spans the primary corridor of AR activity impacting the west coast from northern California to British Columbia, consistent with established AR climatologies (e.g., Guan & Waliser, 2015; Shields et al., 2018). Sensitivity tests using modest shifts in the detection region yielded similar results, indicating that the primary findings are not dependent on the exact placement of this box (not shown). This process converts the AR dataset from hourly to daily resolution, and we refer to these dates as AR detection days.

Following each AR detection day, we track the subsequent 10 days to examine the downstream evolution of surface conditions. However, to isolate periods without direct AR influence over the PNW, we exclude any of these subsequent days if an AR is present within the PNW region (125°–120°W, 42°–52°N; green box in Figure 1).

21698996, 2026, 16, Downloaded from https://agupubs.onlinelibrary.wiley.com/doi/10.1029/2026JD046646, Wiley Online Library on [11/11/2026]. See the Terms and Conditions (https://onlinelibrary.wiley.com/terms-and-conditions) on Wiley Online Library for rules of use; OA articles are governed by the applicable Creative Commons License

21698996, 2026, 16, Downloaded from https://agupubs.onlinelibrary.wiley.com/doi/10.1029/2026JD046646, Wiley Online Library on [11/11/2026]. See the Terms and Conditions (https://onlinelibrary.wiley.com/terms-and-conditions) on Wiley Online Library for rules of use; OA articles are governed by the applicable Creative Commons License

Days on which an AR is present within the PNW are instead cataloged separately as "PNW-AR days." This separation allows us to distinguish between (a) conditions following upstream AR detection and (b) conditions when an AR directly impacts the PNW. This framework is motivated by the meteorological setup preceding the 2021 PNW heatwave, during which an AR remained north of the region prior to the onset of extreme temperatures.

We therefore analyze three categories of days: (a) AR detection days, (b) subsequent days without AR presence in the PNW (up to 10 days after detection), and (c) PNW-AR days. Each category is compared against all other days outside these windows within their respective seasons (DJF or JJA), which serve as the reference period for this analysis.

This dataset was used to find the mean daily maximum temperature (T_{max}), IVT, Z500, total precipitation, and total cloud cover fields during the AR detection days, the following 10 days, and the PNW-AR days as compared to all other days outside this window–the reference period for this analysis.

2.2. Tilted Atmospheric Rivers

To assess how different AR orientations influence summer (JJA) maximum daily temperatures across the PNW, each AR was classified based on the tilt of its IVT structure as it approached the west coast of North America. We hypothesize that more meridionally tilted ARs transport greater amounts of heat from lower latitudes into the PNW. ARs were designated as meridionally tilted (MARs) if their moisture plumes extended from the southwest toward the northeast, and as zonally oriented (ZARs) if they exhibited a more west to east alignment. To quantify these orientations, we computed the tilt angle of the composite IVT field for all AR detection days within the region bounded by 165°–135°W and 35°–55°N (orange box, see Figure S1 in Supporting Information S1 for illustration). The geometric orientation of the composite IVT field was determined using an algorithm that identified the primary axis of the moisture plume and measured its angle relative to east. The resulting principal axis of this composite (average) IVT field is oriented approximately 198.5° counterclockwise from east (red arc in the figure), which serves as the dividing threshold: AR IVT fields with shallower angles are classified as ZARs, and those with steeper angles as MARs.

Using this classification, we extracted the corresponding T_{max}, IVT, Z500, total precipitation, and total cloud cover fields for each MAR and ZAR on the AR detection day and the following 10 days. The reference period comprises all days outside this 11-day window. In analyzing MARs and ZARs, we do not exclude cases where the AR intersects the PNW region, as our goal is to evaluate how meteorological predictability arises from knowing whether an approaching AR is meridional or zonal in orientation. Of the 3,220 JJA days from 1990 to 2024, 277 ARs reached the detection region, of which 91 were classified as MARs and 186 as ZARs. Notably, 40% of MARs and 54% of ZARs eventually intersect the PNW region.

2.3. Statistical Analysis

To determine whether AR-related anomalies of T_{max}, IVT, Z500, total precipitation, and total cloud cover differ meaningfully from conditions without ARs, we use a Welch two-sample *t*-test at each grid point. For each variable, the values on AR detection days (and the following 10 days) are compared with all other days in the season that fall outside this window (the reference period). This produces a map of p-values showing where the AR composites differ from the reference period. Locations where $p > 0.05$ are treated as not statistically significant and are stippled in the figures.

To evaluate how ARs influence regional temperatures, we construct violin plots of the PNW regional-mean T_{max} distribution for the reference period, the AR detection days, the subsequent 10 days, and the PNW-AR days. We apply the same procedure to compare T_{max} distributions associated with MARs and ZARs. To assess whether the overall shapes of the distributions differ, we used the two-sample Kolmogorov–Smirnov (K-S) test. To determine whether specific distributional characteristics—such as the 50th or 90th percentiles—change significantly, we employ a nonparametric bootstrap method in which each distribution is resampled with replacement (10,000 iterations) to estimate the sampling distribution of the percentile difference. A percentile change is significant if the bootstrap indicates a non-zero difference at a 95% confidence level.

21698996, 2026, 16, Downloaded from https://agupubs.onlinelibrary.wiley.com/doi/10.1029/2026JD046646, Wiley Online Library on [11/11/2026]. See the Terms and Conditions (https://onlinelibrary.wiley.com/terms-and-conditions) on Wiley Online Library for rules of use; OA articles are governed by the applicable Creative Commons License

2.4. Multiple Linear Regression

To quantify the relative influence of AR characteristics and large-scale circulation on downstream temperature anomalies, we performed multiple linear regression analyses separately for DJF and JJA AR events. For each event, the PNW regional mean (see green box in Figure S2 in Supporting Information S1) T_{max} anomaly at lag days 0–10 following AR detection was used as the response variable. Predictor variables included the PNW regional mean Z500 anomaly on the corresponding lag day, the upstream regional mean (see orange box in Figure S2 in the Supporting Information S1) AR-day IVT anomaly, the upstream AR-day precipitation anomaly, and a binary AR orientation classification (0 = ZAR, 1 = MAR). Continuous predictors (Z500, IVT, and precipitation) were standardized prior to regression to facilitate comparison of coefficient magnitudes, while the orientation classification was retained as a binary variable to allow direct interpretation of the temperature difference between MAR and ZAR events. Separate regressions were fit for each lag day using ordinary least squares, and regression coefficients, p-values, and model skill metrics (R^2 and adjusted R^2) were recorded. This framework allowed us to assess whether AR orientation contributed to downstream temperature anomalies after accounting for contemporaneous circulation strength and AR intensity.

Portions of the data analysis workflow and manuscript editing were assisted using ChatGPT, a large language model developed by OpenAI. All analyses, interpretations, and conclusions were performed and verified by the authors.

3. Results

3.1. JJA and DJF ARs and the PNW T_{max} Response

The 2021 PNW heatwave has been partially attributed to an atmospheric river (AR) that made landfall north of the region roughly a week before peak temperatures (Mo et al., 2022). As this AR traversed the North Pacific, it transported large amounts of moisture and heat energy and interacted with a pre-existing high-pressure system over western North America. This interaction strengthened the high-pressure ridge, enhancing subsidence and adiabatic warming, which together contributed to the record-breaking heat observed during the event, particularly in British Columbia. Building on this context, we aim to examine maximum daily temperature (T_{max}) anomalies across the PNW under similar AR conditions. Specifically, we identify ARs that make landfall outside the PNW during the JJA and DJF seasons from 1990 to 2024 and analyze meteorological variables as each AR approaches and makes landfall.

Figure 2 (top-left panel) presents the composite mean IVT anomalies associated with ARs reaching the detection region (red box) during JJA. These anomalies are calculated relative to a reference period that excludes AR detection days, the subsequent 10 days (+1 to +10), and any periods when ARs are present within the PNW region. The reference composite therefore represents AR events that do not intersect the PNW region (green box) for up to 10 days following passing through the detection region. As such, by Day +2 (top-middle panel), the IVT pattern reveals a clear bifurcation, with ARs tending to track either north or south of the PNW (odd days, Day +1 through Day +9, can be found in Figure S3 in Supporting Information S1). This departure from a consistent eastward flow corresponds closely with the JJA Z500 anomaly pattern (Figure 3 and Figure S4 in the Supporting Information S1). On the AR detection day, a dipole of negative Z500 anomalies south of Alaska and positive anomalies over the central North Pacific, representing enhancements of the Aleutian Low and the North Pacific High, establishes a narrow corridor of flow through the detection region. However, these Z500 anomalies weaken east of approximately 130°W, leaving no large-scale circulation features to steer the ARs beyond this point. Consequently, after Day +2, the AR pathways diverge, with some systems deflecting northward and others tracking south of the PNW region. This large-scale variance in the Z500 fields over land and the distinction between meridionally tilted and zonally oriented ARs will be explored further in Results 3.2. By Days +4 and +6, IVT anomalies remain significant north of the PNW region before weakening by Days +8 and +10. In contrast, ARs that make landfall directly within the PNW exhibit a pronounced IVT anomaly extending across the North Pacific into the PNW region (Figure 2, bottom-left panel).

Building on the 2021 PNW heatwave—partially attributed to an AR making landfall north of the region (Mo et al., 2022)—we might expect elevated temperatures in the PNW following AR detections in the North Pacific. However, Figure 4 and Figure S5 in the Supporting Information S1 (which shows the corresponding odd days) show that T_{max} anomalies in the PNW are largely insignificant on the AR detection day through Day +10. This

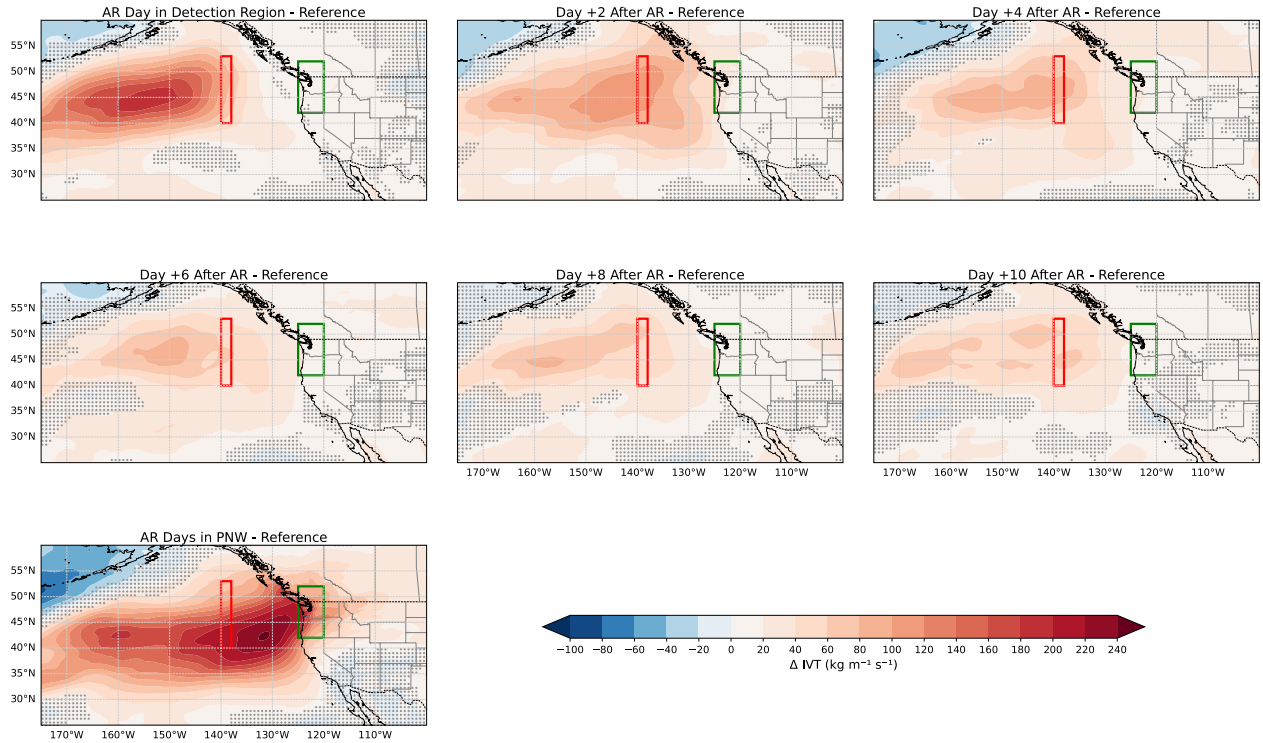


Figure 2. JJA integrated vapor transport anomalies (kg m^{-1} s^{-1}) from the reference composite for composites of the atmospheric river (AR) detection days, the subsequent 10 days (only even days are shown in this figure, odd days are shown in Figure S3 in Supporting Information S1), and the AR events that intersect the Pacific Northwest (PNW) region (green box). The reference composite excludes AR detection days, the subsequent 10 days, and any periods when ARs are present within the PNW region. The red box represents the AR detection region. Stippling represents areas where the anomalies are not significant at 95% confidence.

lack of significance is further supported by the violin plots in Figure S6 in the Supporting Information S1, which show minimal changes across percentiles relative to the reference period (Table 1). We attribute this result to the compositing of ARs that track both north and south of the PNW, effectively averaging out opposing thermal responses. Results 3.2 will address this by distinguishing between these AR pathways. Notably, the only significant temperature response consistent across all percentiles occurs when ARs directly intersect the PNW region, producing a median T_{max} decrease of 2.79°C (Table 1). This cooling is likely associated with the zonal advection of relatively cool, moist marine air inland, along with increased precipitation and cloud cover (Figures S7 and S8 in the Supporting Information S1).

The DJF season contrasts sharply with JJA in the magnitude and spatial coherence of T_{max} anomalies. During DJF, IVT anomalies exhibit a more consistent southwest to northeastward progression from the AR detection day through Day +10 (Figure 5 and Figure S9 in the Supporting Information S1). Notably, significant IVT anomalies are largely confined north of the PNW region, indicating a more uniform, meridionally tilted AR orientation. This configuration aligns with Z500 height anomalies—characterized by low heights south of Alaska and a band of high heights extending from the eastern North Pacific through California to Canada—which together establish geostrophic flow patterns that mirror the IVT tilt (Figure 6 and Figure S10 in the Supporting Information S1). This coherent circulation pattern produces widespread and consistent DJF T_{max} anomalies across the region (Figure 7 and Figure S11 in the Supporting Information S1).

During DJF, ARs are linked to significant positive T_{max} anomalies across the PNW that emerge roughly 2 days after AR detection and persist for at least 10 days. Violin plots (Figure S12 in the Supporting Information S1) highlight this sustained warming, showing statistically significant increases in the 10th, 25th, 50th, and 75th percentiles of T_{max} from Days +2 to +10 (Table 2). The largest anomalies occur in the lower percentiles: the 10th percentile rises by up to 3.0°C for ARs that bypass the PNW and 3.6°C for those that make landfall within the region. In contrast, the 90th percentile remains relatively unchanged for ARs that do not intersect the PNW, indicating that AR-related warming primarily elevates the colder portion of the T_{max} distribution rather than the warm extremes.

21698996, 2026, 16, Downloaded from https://agupubs.onlinelibrary.wiley.com/doi/10.1029/2026JD046646, Wiley Online Library on [11/11/2026]. See the Terms and Conditions (https://onlinelibrary.wiley.com/terms-and-conditions) on Wiley Online Library for rules of use; OA articles are governed by the applicable Creative Commons License

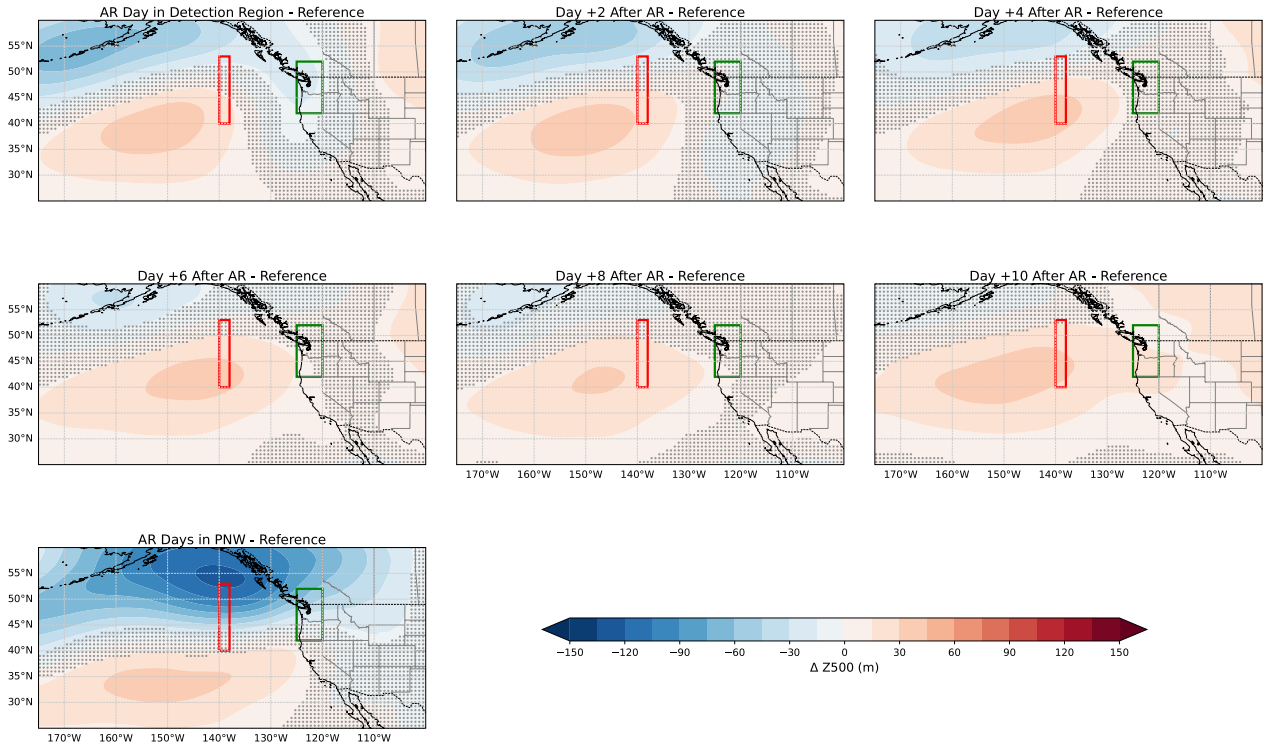


Figure 3. JJA Z500 anomalies (m) from the reference composite for composites of the atmospheric river (AR) detection days, the subsequent 10 days (only even days are shown in this figure, odd days are shown in Figure S4 in Supporting Information S1), and the AR events that intersect the Pacific Northwest (PNW) region (green box). The reference composite excludes AR detection days, the subsequent 10 days, and any periods when ARs are present within the PNW region. The red box represents the AR detection region. Stippling represents areas where the anomalies are not significant at 95% confidence.

These warm anomalies are most pronounced where ARs make landfall in southwestern Canada, north of the PNW, with a broad belt of elevated temperatures extending eastward into Canada and the northern Great Plains. When ARs directly enter the PNW region (Figure 7, bottom-left panel), the mean T_{max} anomaly reaches +2.20°C for the median and +1.12°C for the 90th percentile (Table 2), with localized anomalies exceeding +5°C in Montana. Collectively, these results demonstrate that ARs intersecting the PNW region produce the strongest PNW warming, driven by the advection of relatively warm marine air into the region and corresponding increases in sensible heat convergence and downwelling of longwave radiation (Scholz & Lora, 2024).

3.2. Tilted JJA ARs and the PNW T_{max} Response

The JJA results from Results 3.1 indicate that predicting future PNW T_{max} anomalies in association with an AR detected over the North Pacific is challenging, as individual ARs may track north of, south of, or directly through the PNW region bringing unique meteorological conditions. Here, we address this uncertainty by distinguishing between meridionally tilted ARs (MARs) and zonally oriented ARs (ZARs). As noted in the Methods, we include ARs that intersect the PNW when analyzing MARs and ZARs. Our aim is to assess how much meteorological predictability can be gained simply from knowing whether an approaching AR has a meridional or zonal orientation.

To classify these events, we first construct a composite mean of all ARs at the time they reach the detection region (Figure S1 in the Supporting Information S1) and measure the angle of the IVT "blob" within the domain bounded by 165°–135°W and 35°–55°N (orange box). ARs with IVT angles steeper than the composite mean are categorized as MARs, while those with shallower angles are designated as ZARs. 33% of JJA ARs passing through the detection region are classified as MARs and 67% are ZARs. (On the other hand, using the JJA-derived orientation threshold, 66% of DJF ARs would be classified as more meridionally oriented (MAR-like), while 34% are more zonal (ZAR-like).)

21698996, 2026, 16, Downloaded from https://agupubs.onlinelibrary.wiley.com/doi/10.1029/2026JD046646, Wiley Online Library on [11/11/2026]. See the Terms and Conditions (https://onlinelibrary.wiley.com/terms-and-conditions) on Wiley Online Library for rules of use; OA articles are governed by the applicable Creative Commons License

21698996, 2026, 16, Downloaded from https://agupubs.onlinelibrary.wiley.com/doi/10.1029/2026JD046646, Wiley Online Library on [11/11/2026]. See the Terms and Conditions (https://onlinelibrary.wiley.com/terms-and-conditions) on Wiley Online Library for rules of use; OA articles are governed by the applicable Creative Commons License

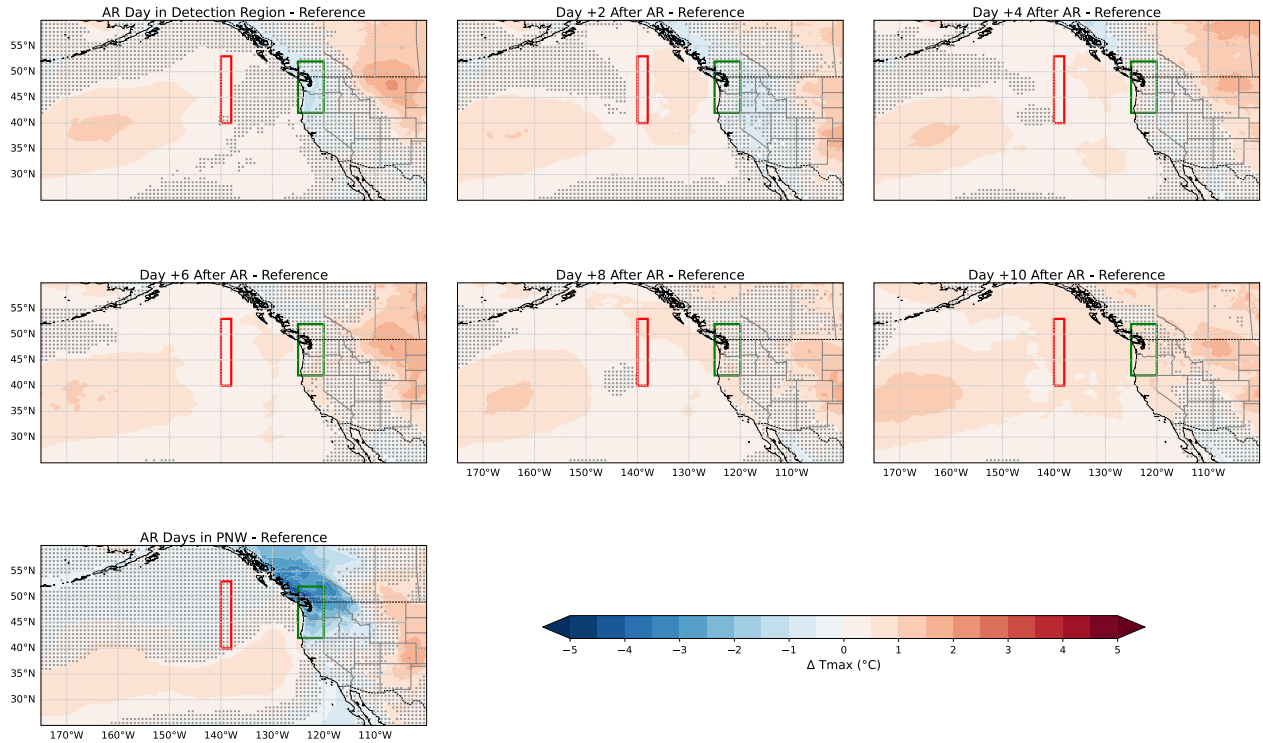


Figure 4. JJA daily maximum temperature (T_{max}) anomalies (°C) from the reference composite for composites of the atmospheric river (AR) detection days, the subsequent 10 days (only even days are shown in this figure, odd days are shown in Figure S5 in Supporting Information S1), and the AR events that intersect the Pacific Northwest (PNW) region (green box). The reference composite excludes AR detection days, the subsequent 10 days, and any periods when ARs are present within the PNW region. The red box represents the AR detection region. Stippling represents areas where the anomalies are not significant at 95% confidence.

As expected, when compared to the reference period (days outside of the AR detection day and the subsequent 10 days), MARs exhibit stronger poleward moisture transport than ZARs (Figure 8 shows the AR detection day and Days +1–4; Days +5–10 are provided in Figure S13 in the Supporting Information S1). This enhanced

Table 1
PNW Regional Mean JJA Daily Maximum Temperature (T_{max}) Anomalies (°C) per Percentile From the Reference Composite for Composites of the AR Detection Days (AR Day), the Subsequent 10 Days (Day +1 Through Day +10), and the AR Events That Intersect the PNW Region (AR in PNW)

	K-S Stat	10th %ile	25th %ile	50th %ile	75th %ile	90th %ile
AR Day	0.09	−0.83	−0.55	**−0.78**	−0.68	**−0.68**
Day +1	**0.10**	−0.87	−0.42	**−0.65**	**−0.83**	**−1.09**
Day +2	0.05	−0.64	−0.41	−0.29	−0.15	−0.38
Day +3	0.06	−0.12	0.00	−0.44	0.44	0.21
Day +4	0.06	0.15	−0.19	0.30	0.34	0.64
Day +5	0.04	0.17	0.08	0.25	0.59	0.32
Day +6	0.08	0.31	0.30	0.40	0.32	0.43
Day +7	0.06	0.45	0.37	0.04	0.17	0.34
Day +8	0.06	0.12	0.38	0.13	0.61	0.42
Day +9	0.08	0.33	0.38	0.39	0.29	0.60
Day +10	**0.11**	0.63	0.59	0.98	0.63	0.78
AR in PNW	**0.27**	**−1.92**	**−2.43**	**−2.79**	**−3.08**	**−2.57**

Note. The reference composite excludes AR detection days, the subsequent 10 days, and any periods when ARs are present within the PNW region. Also listed is the two-sample Kolmogorov–Smirnov (K-S) test statistics to determine whether the overall shapes of the distributions differ (unitless). Significant changes at 95% confidence are in bold text, see Methods for further details. For a visualization of this data, please refer to the violin plots in Figure S6 in the Supporting Information S1.

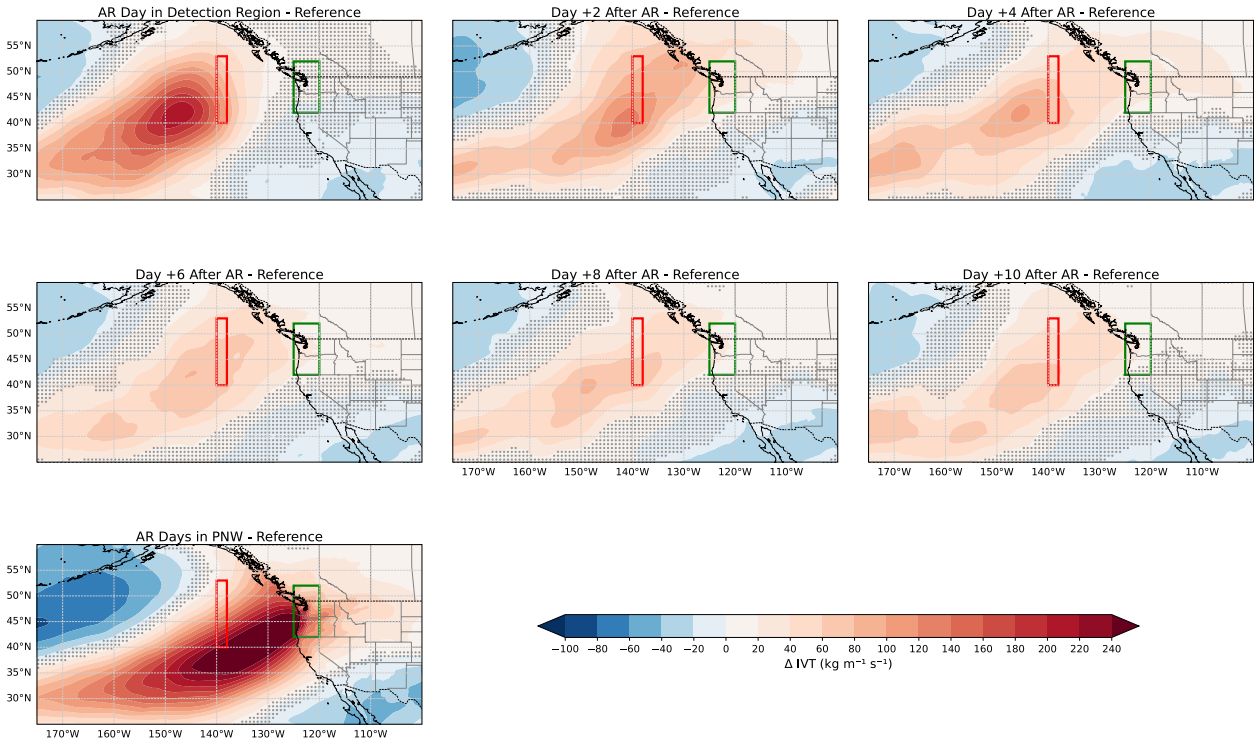


Figure 5. DJF integrated vapor transport anomalies (kg m^{-1} s^{-1}) from the reference composite for composites of the atmospheric river (AR) detection days, the subsequent 10 days (only even days are shown in this figure, odd days are shown in Figure S9 in Supporting Information S1), and the AR events that intersect the Pacific Northwest (PNW) region (green box). The reference composite excludes AR detection days, the subsequent 10 days, and any periods when ARs are present within the PNW region. The red box represents the AR detection region. Stippling represents areas where the anomalies are not significant at 95% confidence.

transport reflects the influence of the MAR Z500 anomaly pattern, which tilts northeastward across the North Pacific, featuring a low-pressure anomaly near southern Alaska and a high-pressure anomaly extending from the central North Pacific toward the PNW region (Figure 9 and Figure S14 in the Supporting Information S1). In contrast, the ZAR Z500 anomalies tilt southeastward, with a low centered from Alaska to the PNW and a high anomaly located over the central North Pacific. The resulting difference field (MARs–ZARs; right column of Figure 9) reveals a relative ridge adjacent to the PNW that both steers MARs toward the region and southwestern Canada and fosters elevated T_{max} anomalies through enhanced subsidence and associated warming.

Figure 10 and Figure S15 in the Supporting Information S1 present the T_{max} anomalies associated with MARs and ZARs. Relative to the reference period, MARs produce significant positive T_{max} anomalies over the PNW beginning around 2 days after AR detection and persisting through Day +3. In contrast, ZARs are linked to negative T_{max} anomalies across the PNW that remain significant from the AR detection day through Day +3. The pronounced cold anomalies observed on the detection day and Day +1—preceding AR landfall—arise from the pre-existing atmospheric structure, characterized by a southeastward-tilting geostrophic flow from Alaska toward the PNW (Figure 9). As a result, cold air is advected into the region prior to AR landfall. It is also important to note that ZARs bring more total cloud cover to the PNW region as compared to MARs, which likely contributes to the cooling signal associated with ZARs (Figure S16 in the Supporting Information S1).

When comparing MARs to ZARs (MARs–ZARs), T_{max} anomalies over the PNW are largely significant from Day +1 through Day +4, with localized warming exceeding 3.5°C on Day +2 (Figure 10). This spatial pattern is consistent with the statistical distributions shown in the violin plots (Figure 11) and summarized in Table 3, which indicate a significant increase in the 50th percentile T_{max} during the same period. Notably, the extreme temperature response is also evident: on Days +2 and +3, the 90th percentile T_{max} increases significantly by +2.17° and +1.44°C, respectively, highlighting a broader upward shift across the temperature distribution during MAR events as compared to ZAR events.

21698996, 2026, 16, Downloaded from https://agupubs.onlinelibrary.wiley.com/doi/10.1029/2026JD046646, Wiley Online Library on [11/11/2026]. See the Terms and Conditions (https://onlinelibrary.wiley.com/terms-and-conditions) on Wiley Online Library for rules of use; OA articles are governed by the applicable Creative Commons License

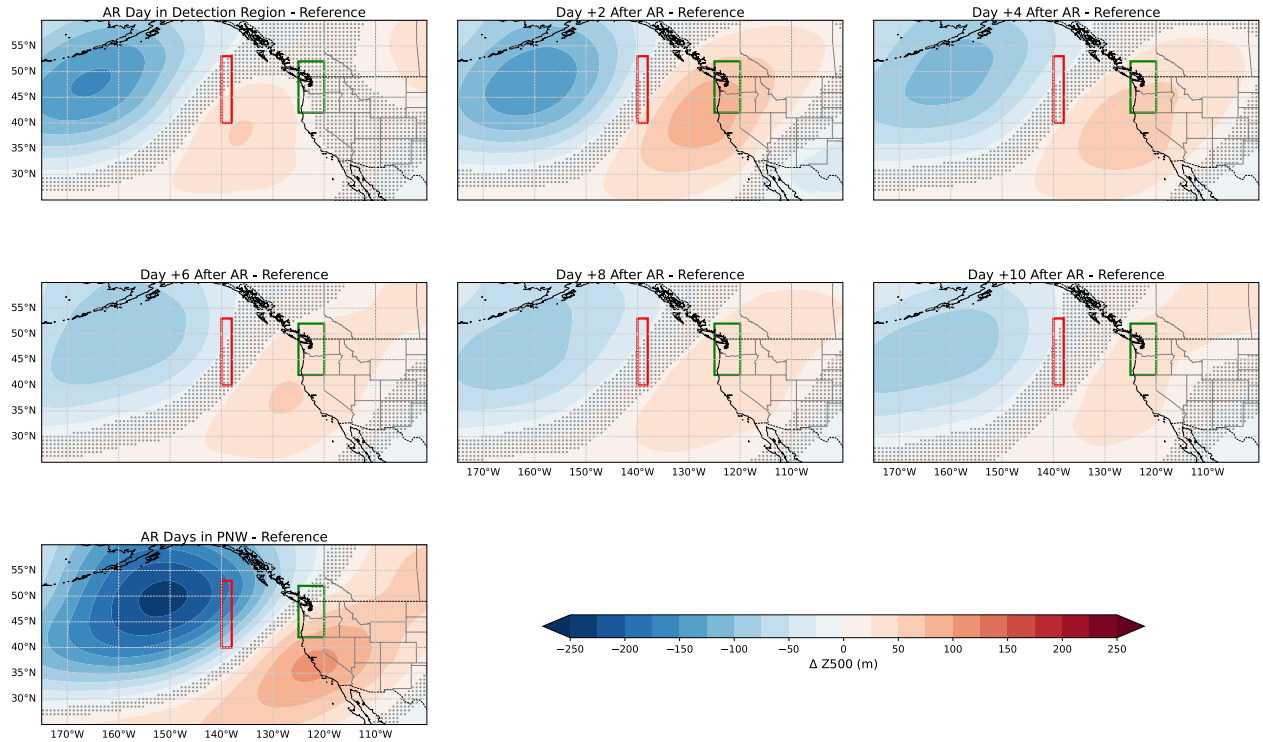


Figure 6. DJF Z500 anomalies (m) from the reference composite for composites of the atmospheric river (AR) detection days, the subsequent 10 days (only even days are shown in this figure, odd days are shown in Figure S10 in Supporting Information S1), and the AR events that intersect the Pacific Northwest (PNW) region (green box). The reference composite excludes AR detection days, the subsequent 10 days, and any periods when ARs are present within the PNW region. The red box represents the AR detection region. Stippling represents areas where the anomalies are not significant at 95% confidence.

Figure 11's violin plots also indicate the T_{max} values associated with the 2021 PNW heatwave (green stars; AR detection day: 22 June 2021). These markers show that the peak T_{max} during the 2021 event occurred after the Day +2 to +3 window, when MARs exhibit their strongest anomalies relative to the reference period. This timing underscores the exceptional nature of the 2021 heatwave and suggests that additional factors beyond AR-related moisture and heat transport contributed to its intensity.

3.3. Multiple Linear Regression

To assess the relative roles of dynamics versus thermodynamics in the AR-associated intensification of heat anomalies, we perform a multiple linear regression on T_{max}, with dynamics being represented by Z500 (associated with subsidence-driven warming) and AR angle (associated with meridional heat transport) and thermodynamics being represented by upstream precipitation (net latent heat release into the column) and moisture transport (see Methods 3.4 for details).

Multiple linear regression analysis reveals that Z500 anomalies are the dominant predictor of T_{max} anomalies following atmospheric river events in both seasons (Table 4 and Figure 12). In DJF, standardized Z500 coefficients range from 1.21 to 1.73 and are statistically significant at all lags, while model R^2 values range from 0.16 to 0.29. Precipitation anomalies are negatively associated with T_{max} during the first several days following AR detection, with significant coefficients at lags 1–3, suggesting that enhanced cloudiness and precipitation may suppress daytime warming. By contrast, IVT anomalies exhibit weak and generally insignificant relationships with T_{max}. AR orientation shows positive coefficients through lag day 4, indicating that MAR-like events tend to be warmer than ZAR-like events after controlling for Z500, IVT, and precipitation, although these differences are generally not statistically significant.

The influence of Z500 is substantially stronger during JJA (Table 4 and Figure 12), with standardized coefficients near 4.0 at all lags and R^2 values exceeding 0.85, indicating that contemporaneous ridge strength explains most of the variance in T_{max} anomalies. Despite the dominant role of Z500, AR orientation retains an independent

21698996, 2026, 16, Downloaded from https://agupubs.onlinelibrary.wiley.com/doi/10.1029/2026JD046646, Wiley Online Library on [11/11/2026]. See the Terms and Conditions (https://onlinelibrary.wiley.com/terms-and-conditions) on Wiley Online Library for rules of use; OA articles are governed by the applicable Creative Commons License

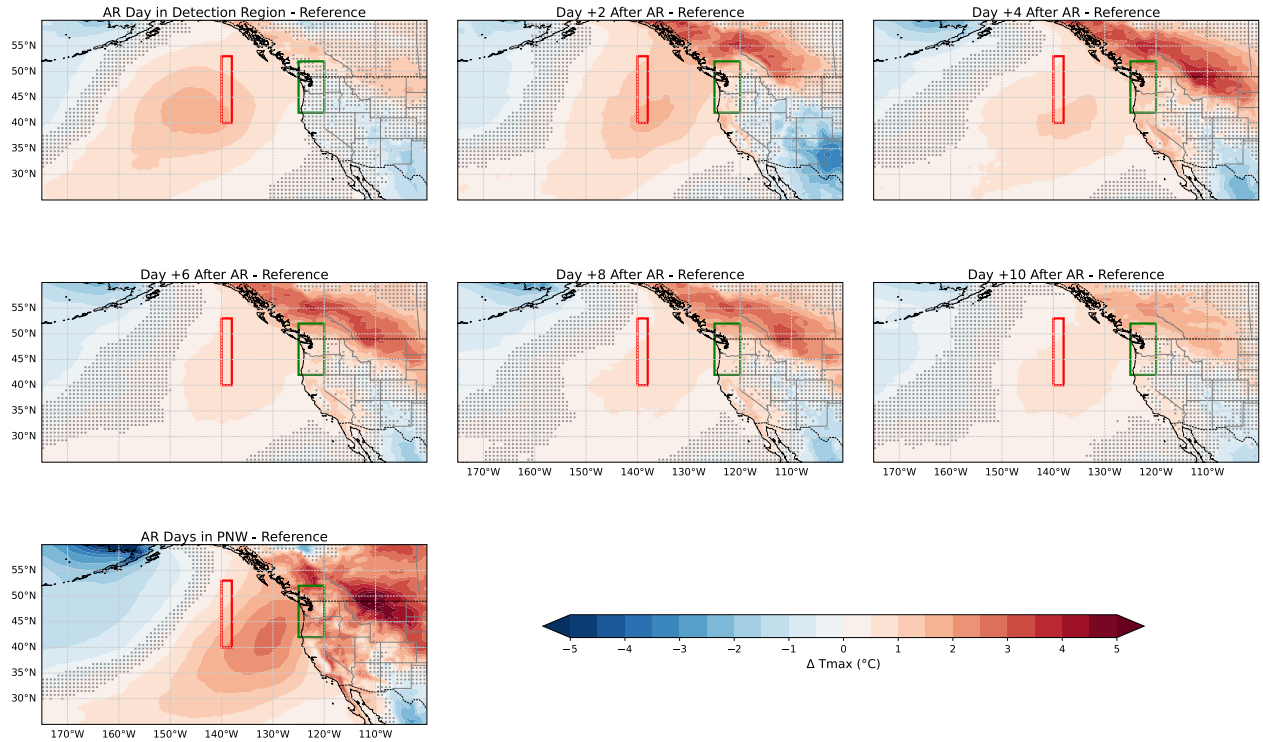


Figure 7. DJF daily maximum temperature (T_{max}) anomalies (°C) from the reference composite for composites of the atmospheric river (AR) detection days, the subsequent 10 days (only even days are shown in this figure, odd days are shown in Figure S11 in Supporting Information S1), and the AR events that intersect the Pacific Northwest (PNW) region (green box). The reference composite excludes AR detection days, the subsequent 10 days, and any periods when ARs are present within the PNW region. The red box represents the AR detection region. Stippling represents areas where the anomalies are not significant at 95% confidence.

influence on summer temperatures. After accounting for Z500, IVT, and precipitation anomalies, MAR events are associated with significantly warmer T_{max} anomalies than ZAR events at lag days 3 and 4, with coefficients of 0.46°C ($p = 0.04$) and 0.59°C ($p = 0.01$), respectively. The orientation effect is weak or insignificant at other lags.

Table 2
PNW Regional Mean DJF Daily Maximum Temperature (T_{max}) Anomalies (°C) per Percentile From the Reference Composite for Composites of the AR Detection Days (AR Day), the Subsequent 10 Days (Day +1 Through Day +10), and the AR Events That Intersect the PNW Region (AR in PNW)

	KS Stat	10th %ile	25th %ile	50th %ile	75th %ile	90th %ile
AR Day	0.09	**1.98**	0.54	0.23	−0.39	**−0.93**
Day +1	0.09	1.77	0.57	0.49	−0.29	**−1.01**
Day +2	**0.16**	**2.08**	**1.48**	**1.21**	**0.54**	−0.15
Day +3	**0.21**	**2.33**	**1.64**	**1.41**	**0.63**	−0.07
Day +4	**0.20**	**3.02**	**1.82**	**1.40**	**1.11**	0.35
Day +5	**0.20**	**2.02**	**1.43**	**1.28**	**1.00**	0.39
Day +6	**0.18**	**2.02**	**1.18**	**1.33**	**0.73**	−0.04
Day +7	**0.21**	**2.09**	**1.49**	**1.40**	**0.83**	0.36
Day +8	**0.17**	**1.88**	**1.14**	**1.24**	**0.68**	0.04
Day +9	**0.16**	**2.28**	**1.43**	**0.96**	**0.69**	−0.22
Day +10	**0.14**	**2.25**	**1.25**	**0.85**	**0.49**	0.14
AR in PNW	**0.30**	**3.58**	**2.76**	**2.20**	**1.60**	**1.12**

Note. The reference composite excludes AR detection days, the subsequent 10 days, and any periods when ARs are present within the PNW region. Also listed is the two-sample Kolmogorov–Smirnov (K-S) test statistics to determine whether the overall shapes of the distributions differ (unitless). Significant changes at 95% confidence are in bold text, see Methods for further details. For a visualization of this data, please refer to the violin plots in Figure S12 in the Supporting Information S1.

21698996, 2026, 16, Downloaded from https://agupubs.onlinelibrary.wiley.com/doi/10.1029/2026JD046646, Wiley Online Library on [11/11/2026]. See the Terms and Conditions (https://onlinelibrary.wiley.com/terms-and-conditions) on Wiley Online Library for rules of use; OA articles are governed by the applicable Creative Commons License

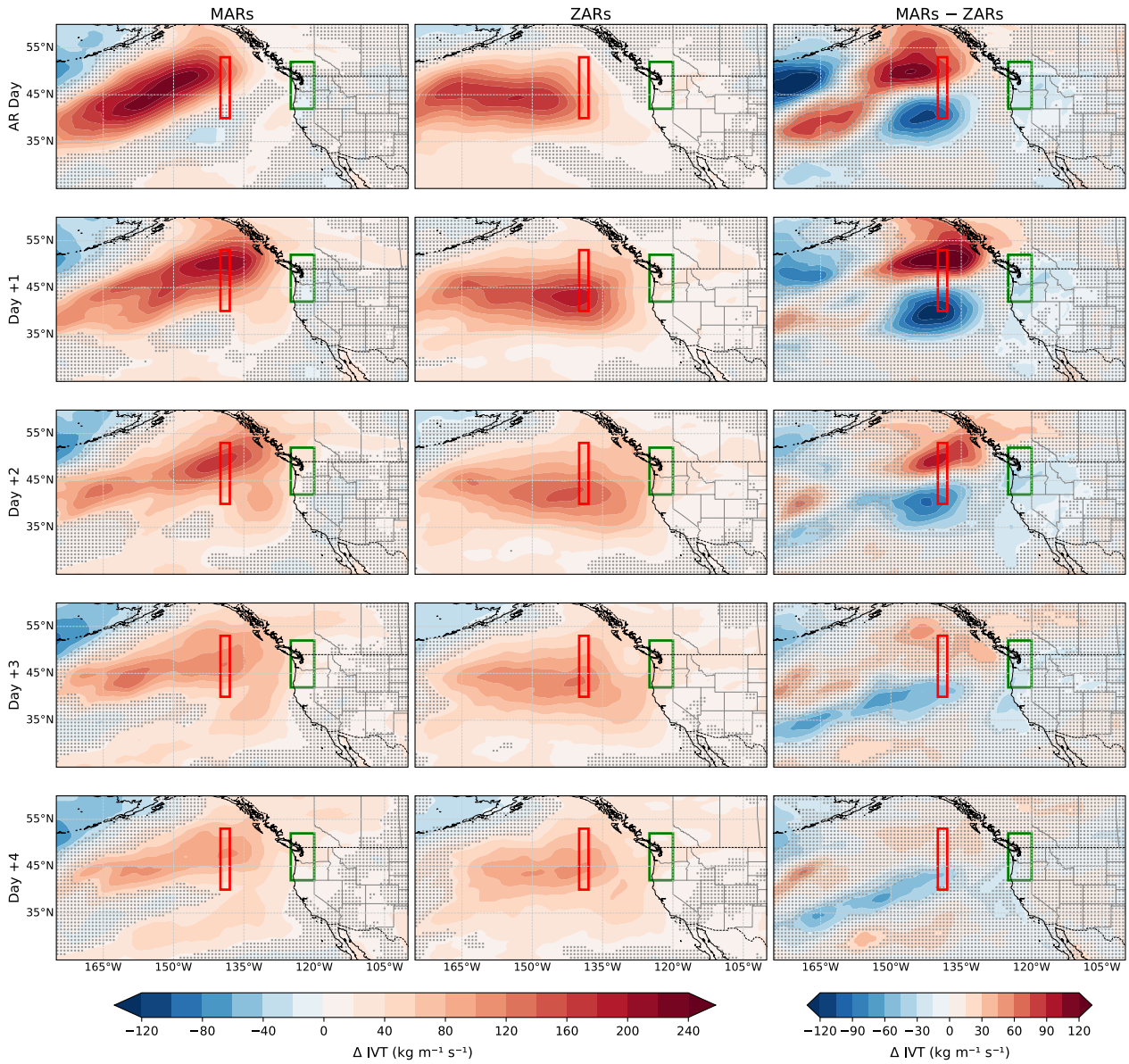


Figure 8. JJA MARs (first column) and ZARs (second column) composites of integrated vapor transport (IVT) (kg m^{-1} s^{-1}) relative to the reference composite (days outside the atmospheric river (AR) detection day and the subsequent 10 days) for the AR detection day through +4 days after the detection day (Day +5 through +10 can be found in Figure S13 in the Supporting Information S1). The third column shows MARs minus ZARs composite IVT. The red box represents the AR detection region, and the green box outlines the Pacific Northwest region. Stippling represents areas where the anomalies are not significant at 95% confidence.

Precipitation anomalies transition from weakly negative coefficients at short lags to significantly positive coefficients at days 3–4, whereas IVT anomalies are generally small and inconsistent in sign. Together, these results suggest that while downstream temperature anomalies are primarily controlled by large-scale ridging, AR orientation provides additional predictive information regarding summertime warming several days after AR landfall.

4. Discussion

Recent studies have increasingly recognized that ARs are not only critical conduits of moisture but also major agents of heat transport and surface warming. Scholz and Lora (2024) demonstrate that ARs deliver substantial sensible and latent heat into the regions where they make landfall, producing widespread warm temperature anomalies—often exceeding +5°C above the climatology—and accounting for more than two-thirds of extreme

21698996, 2026, 16, Downloaded from https://agupubs.onlinelibrary.wiley.com/doi/10.1029/2026JD046646, Wiley Online Library on [11/11/2026]. See the Terms and Conditions (https://onlinelibrary.wiley.com/terms-and-conditions) on Wiley Online Library for rules of use; OA articles are governed by the applicable Creative Commons License

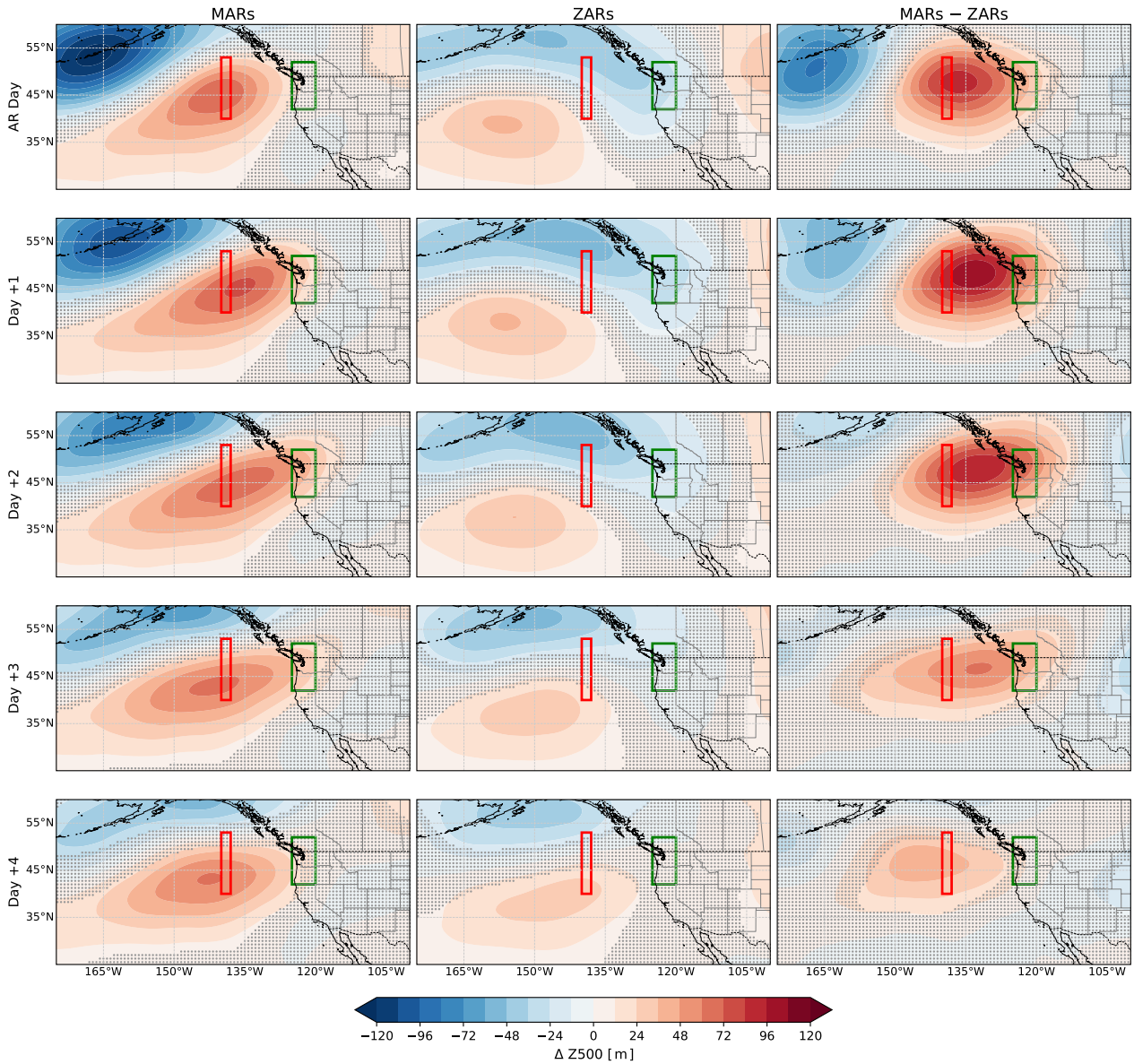


Figure 9. JJA MARs (first column) and ZARs (second column) composites of Z500 (m) relative to the reference composite (days outside the atmospheric river (AR) detection day and the subsequent 10 days) for the AR detection day through +4 days after the detection day (Day +5 through +10 can be found in Figure S14 in the Supporting Information S1). The third column shows MARs minus ZARs composite Z500. The red box represents the AR detection region, and the green box outlines the Pacific Northwest region. Stippling represents areas where the anomalies are not significant at 95% confidence.

warm events across much of the mid-latitudes. This large-scale warming effect complements the findings of Gonzales et al. (2019), who report a 0.7°–1.6°C increase in the mean temperature of landfalling ARs along the U.S. West Coast during the cool season over recent decades, implying that the thermal properties of ARs themselves are intensifying under contemporary climate change. Consistent with these observations, Shields et al. (2019) show that ARs act as efficient carriers of meridional heat, transporting both latent and sensible energy poleward, with the latent component projected to strengthen in a warmer climate. Together, these studies underscore that ARs are thermodynamic as well as hydrologic phenomena—capable of redistributing heat and modifying surface energy budgets over continental margins. Our results extend this understanding to the PNW, revealing that the thermal influence of ARs depends strongly on their orientation and seasonality: winter (DJF) ARs with coherent meridional structure consistently warm the region, while summer (JJA) warming emerges only when ARs exhibit a pronounced poleward tilt (MARs). These findings indicate that AR geometry—and its

21698996, 2026, 16, Downloaded from https://agupubs.onlinelibrary.wiley.com/doi/10.1029/2026JD046646, Wiley Online Library on [11/11/2026]. See the Terms and Conditions (https://onlinelibrary.wiley.com/terms-and-conditions) on Wiley Online Library for rules of use; OA articles are governed by the applicable Creative Commons License

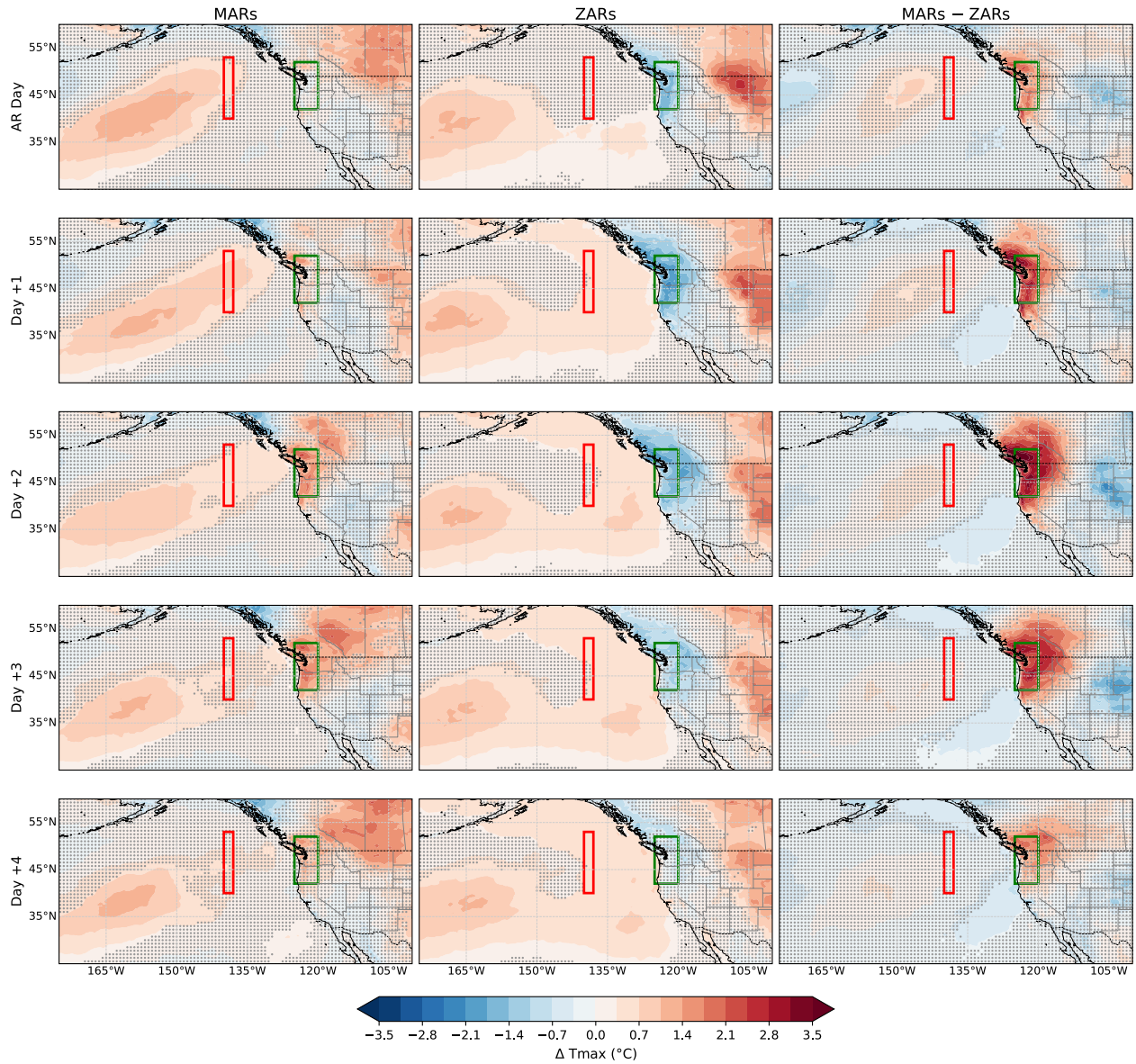


Figure 10. JJA MARs (first column) and ZARs (second column) composites of daily maximum temperature (T_{max}, °C) relative to the reference composite (days outside the atmospheric river (AR) detection day and the subsequent 10 days) for the AR detection day through +4 days after the detection day (Day +5 through +10 can be found in Figure S15 in the Supporting Information S1). The third column shows MARs minus ZARs composite T_{max}. The red box represents the AR detection region, and the green box outlines the Pacific Northwest region. Stippling represents areas where the anomalies are not significant at 95% confidence.

associated modulation of meridional heat transport—plays an important role in determining whether ARs act as precursors to regional warming or as neutral/cooling events.

Although our analysis demonstrates clear seasonal and geometric differences in AR-induced warming, additional work is needed to determine the physical mechanisms responsible for these temperature responses—particularly whether they arise primarily from advective heating or from latent heating. Evidence from the 2021 PNW heatwave suggests that both pathways may play important roles. During that event, an unusually intense AR approaching southeast Alaska contributed substantial moisture and heat to the developing ridge, and rapid increases in water vapor enhanced local radiative heating (Lin et al., 2022; Mo et al., 2022). Several studies have shown that this upstream diabatic heating influenced the amplitude and position of the blocking ridge, as well as the properties of the air mass that ultimately descended over the PNW (Neal et al., 2022; Papritz & Röthlisberger, 2023; White et al., 2023). Understanding whether similar processes operate during JJA MARs or winter

21698996, 2026, 16, Downloaded from https://agupubs.onlinelibrary.wiley.com/doi/10.1029/2026JD046646, Wiley Online Library on [11/11/2026]. See the Terms and Conditions (https://onlinelibrary.wiley.com/terms-and-conditions) on Wiley Online Library for rules of use; OA articles are governed by the applicable Creative Commons License

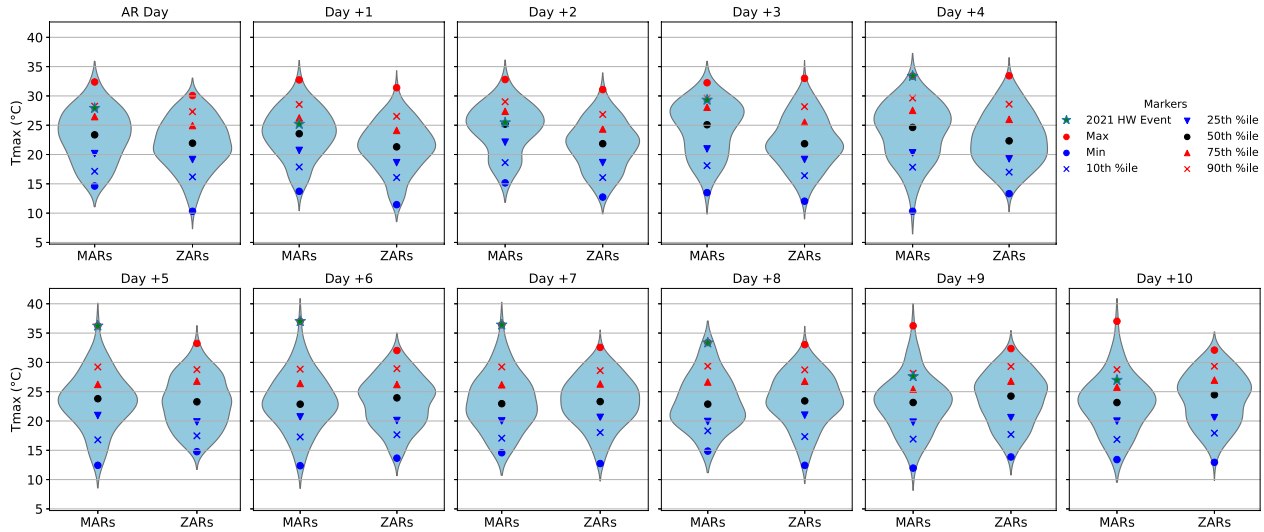


Figure 11. JJA violin plots of the Pacific Northwest (PNW) regional mean T_{max} distribution for the MARs and ZARs composites during the atmospheric river (AR) detection days and the subsequent 10 days. The markers show the maximum, minimum, and various percentiles for the distributions as well as a green star indicating the T_{max} values associated with the 2021 PNW heatwave whose AR detection day was 22 June 2021. Please refer to Table 3 in the main text for the difference between the MARs and ZARs composites for each of the percentiles and whether the relative difference is statistically significant.

ARs will require targeted diagnostics—such as moist static energy budgets—to separate the contributions of warm-air advection from those of latent heat release. Establishing the relative importance of these mechanisms is critical for interpreting the synoptic controls on AR-driven warming and for anticipating how they may evolve in a changing climate.

Clarifying the balance between advective and latent heating could help explain why ARs warm the PNW in some situations but not in others. This context is especially relevant to our first key result: JJA atmospheric rivers alone do not produce consistent warming across the PNW. When all summer AR events are composited together, there is no clear evidence that they generate warmer daily maximum temperatures in the PNW (Figure 4 and Figures S5 and S6 of the Supporting Information S1). This muted regional response reflects the averaging of ARs that follow divergent trajectories—some tracking north of the PNW, others passing to the south (Figure 2, top-middle panel). These opposing pathways introduce thermal effects that largely cancel in the composite mean, concealing the

Table 3
PNW Regional Mean JJA Daily Maximum Temperature (T_{max}) Anomalies (°C) per Percentile for the MARs Composite Minus the ZARs Composite During the AR Detection Days (AR Day) and the Subsequent 10 Days (Day +1 Through Day +10)

	K-S Stat	10th %ile	25th %ile	50th %ile	75th %ile	90th %ile
AR Day	**0.18**	0.95	1.01	**1.43**	**1.52**	0.94
Day +1	**0.25**	1.80	**2.09**	**2.24**	**2.13**	**2.03**
Day +2	**0.36**	**2.56**	3.48	**3.35**	**3.02**	**2.17**
Day +3	**0.30**	**1.71**	1.80	**3.24**	**2.55**	**1.44**
Day +4	**0.21**	0.84	1.02	**2.30**	1.53	1.05
Day +5	0.11	−0.68	1.09	0.53	−0.56	0.45
Day +6	0.12	−0.38	0.62	−1.08	0.18	−0.09
Day +7	0.09	−0.98	−0.60	−0.36	−0.13	0.62
Day +8	0.16	0.98	−1.08	−0.55	−0.13	0.64
Day +9	0.17	−0.79	−0.77	−1.09	**−1.37**	−1.15
Day +10	0.16	−1.08	−0.59	−1.33	−1.20	−0.58

Note. Also listed is the two-sample Kolmogorov–Smirnov (K-S) test statistics to determine whether the overall shapes of the composite distributions differ (unitless). Significant changes at 95% confidence are in bold text, see Methods for further details. For a visualization of this data, please refer to the violin plots in Figure 11.

21698996, 2026, 16, Downloaded from https://agupubs.onlinelibrary.wiley.com/doi/10.1029/2026JD046646, Wiley Online Library on [11/11/2026]. See the Terms and Conditions (https://onlinelibrary.wiley.com/terms-and-conditions) on Wiley Online Library for rules of use; OA articles are governed by the applicable Creative Commons License

21698996, 2026, 16, Downloaded from https://agupubs.onlinelibrary.wiley.com/doi/10.1029/2026JD046646, Wiley Online Library on [11/11/2026]. See the Terms and Conditions (https://onlinelibrary.wiley.com/terms-and-conditions) on Wiley Online Library for rules of use; OA articles are governed by the applicable Creative Commons License

Table 4
Results of Multiple Linear Regression Analyses Relating PNW T_{max} Anomalies to Contemporaneous Z500 Anomalies, AR-Day Precipitation Anomalies, AR-Day IVT Anomalies, and AR Orientation for Atmospheric River Events During DJF and JJA

Season	lag	r2	adj_r2	coef_z500	coef_tp	coef_ivt	coef_orientation
DJF	0	0.22	0.21	**1.52**	−0.34	0.03	0.38
DJF	1	0.25	0.23	**1.65**	**−0.87**	0.28	0.54
DJF	2	0.19	0.17	**1.43**	**−1.06**	0.48	0.74
DJF	3	0.16	0.14	**1.21**	**−0.71**	0.44	0.83
DJF	4	0.2	0.19	**1.47**	−0.38	0.22	0.45
DJF	5	0.24	0.22	**1.68**	0.09	−0.03	0.12
DJF	6	0.28	0.27	**1.73**	**0.57**	−0.39	0.06
DJF	7	0.27	0.26	**1.62**	**0.68**	**−0.57**	−0.72
DJF	8	0.26	0.24	**1.56**	**0.66**	−0.45	−0.47
DJF	9	0.28	0.26	**1.5**	**0.52**	−0.14	−0.28
DJF	10	0.29	0.27	**1.64**	**0.54**	−0.31	0.00
JJA	0	0.88	0.87	**4.08**	−0.17	0.11	−0.37
JJA	1	0.87	0.86	**3.97**	**−0.40**	**0.23**	−0.33
JJA	2	0.88	0.87	**3.97**	−0.10	−0.08	0.13
JJA	3	0.88	0.88	**4.14**	**0.23**	**−0.26**	**0.46**
JJA	4	0.87	0.87	**4.23**	**0.32**	**−0.32**	**0.59**
JJA	5	0.86	0.86	**4.11**	0.05	−0.20	0.23
JJA	6	0.86	0.86	**4.08**	0.01	−0.17	0.07
JJA	7	0.87	0.87	**4.03**	0.01	−0.06	−0.22
JJA	8	0.86	0.86	**4.1**	0.00	−0.06	−0.15
JJA	9	0.85	0.85	**4.02**	0.08	**−0.27**	0.10
JJA	10	0.89	0.88	**4.15**	0.05	**−0.25**	0.07

Note. Separate regressions were performed for lag days 0–10 following AR detection. Continuous predictors (Z500, TP, and IVT) were standardized prior to regression, while AR orientation was represented as a binary variable (0 = ZAR, 1 = MAR). Reported coefficients therefore represent the change in T_{max} anomaly associated with a one standard deviation increase in the continuous predictor, while the orientation coefficient represents the adjusted T_{max} difference between MAR and ZAR events. The table also includes the coefficient of determination (R^2), adjusted R^2, and significant coefficients at $p < 0.05$ are in bold text, see Methods for further details.

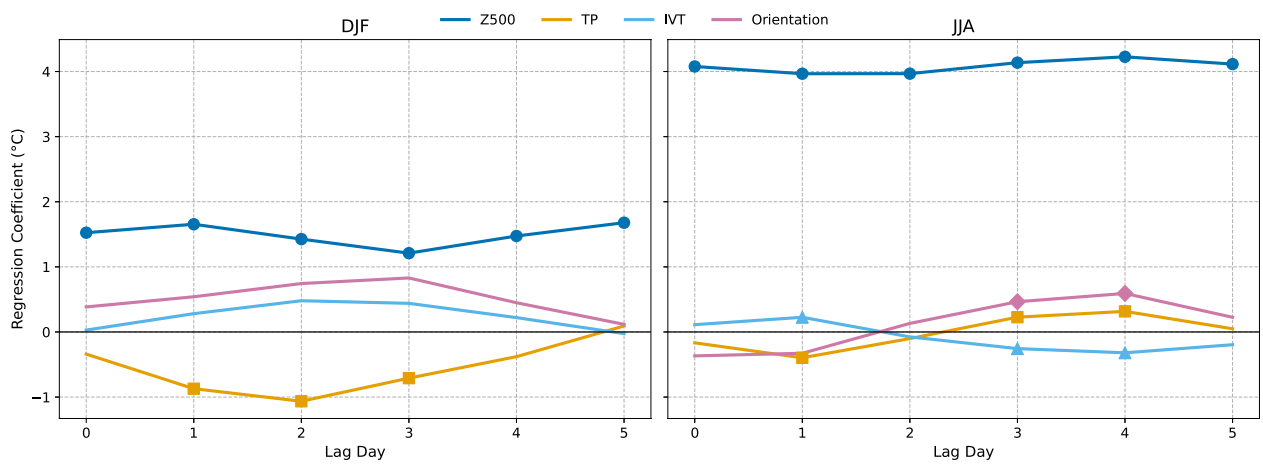


Figure 12. Multiple linear regression coefficients relating T_{max} anomalies to contemporaneous Z500 anomalies, atmospheric river (AR)-day precipitation anomalies, AR-day integrated vapor transport (IVT) anomalies, and AR orientation for DJF (left) and JJA (right) atmospheric river events. Separate regressions were performed for lag days 0–5 following AR detection. Continuous predictors (Z500, TP, and IVT) were standardized prior to regression, while AR orientation was represented as a binary variable (0 = ZAR, 1 = MAR). Markers indicate coefficients that are statistically significant at the 95% confidence level ($p < 0.05$).

21698996, 2026, 16, Downloaded from https://agupubs.onlinelibrary.wiley.com/doi/10.1029/2026JD046646, Wiley Online Library on [11/11/2026]. See the Terms and Conditions (https://onlinelibrary.wiley.com/terms-and-conditions) on Wiley Online Library for rules of use; OA articles are governed by the applicable Creative Commons License

underlying dynamical variability among events. Because the thermal impact of an AR depends heavily on its track and orientation, compositing all JJA ARs together masks the distinct thermodynamic regimes that arise when ARs are meridionally tilted versus when they are zonally aligned. Distinguishing ARs by geometry is therefore essential to reveal how synoptic structure modulates PNW temperature anomalies.

In contrast, wintertime ARs consistently warm the PNW due to their coherent meridional structure. During DJF, ARs tend to exhibit a uniform southwest to northeast orientation, characterized by moisture fluxes and circulation anomalies that favor persistent poleward and inland transport of warm, humid air (Figures 5 and 6). This coherent structure establishes geostrophic flow patterns that enhance both sensible and latent heat advection into the PNW, producing widespread and statistically significant T_{max} anomalies that reach up to +2°C and persist for nearly 10 days following AR detection (Figure 7 and Figures S11 and S12 of the Supporting Information S1). The consistent tilt and alignment of DJF ARs thus explain their stronger and more spatially coherent thermal influence compared to the more variable JJA ARs. This seasonal contrast underscores how the background circulation—particularly the winter jet's meridional orientation—amplifies the capacity of ARs to warm mid-latitude continental regions.

Another key finding is that among JJA events, meridionally tilted ARs drive much stronger PNW warming than zonally oriented ARs. When JJA ARs are separated by orientation, the resulting composites reveal a clear divergence in their thermal impact: MARs are associated with pronounced warming, while ZARs are linked to cooling. MARs elevate median T_{max} by roughly 2.2°–3.4°C relative to ZARs during Days +1 to +4 (Figure 10 and Table 3). This enhanced warming is tied to the MAR-associated synoptic pattern—a northeastward-tilted ridge downstream of the AR that promotes subsidence, adiabatic warming, and sustained poleward moisture transport into the region (Figure 9). By contrast, ZARs reinforce more zonal flow and favor the advection of cooler marine air into the PNW, yielding negative temperature anomalies. These results suggest that AR geometry contributes to the sign and magnitude of surface temperature responses during summer, with meridionally tilted and zonally oriented ARs associated with contrasting temperature outcomes.

The regression results provide additional insight into the mechanisms linking atmospheric rivers to downstream temperature anomalies in the PNW. Consistent with expectations, Z500 anomalies emerged as the dominant predictor of T_{max} anomalies in both seasons, highlighting the importance of large-scale circulation and ridge strength in controlling surface temperatures (Table 4 and Figure 12). The substantially larger Z500 coefficients and higher R^2 values during JJA suggest that summertime temperature variability associated with ARs is more tightly coupled to synoptic-scale ridging than in winter. This finding is consistent with previous studies of the 2021 PNW heatwave, which emphasized the critical role of an amplified upper-level ridge in producing extreme surface temperatures (Mo et al., 2022; Neal et al., 2022; White et al., 2023).

The regression results also suggest a role for latent heating in AR-driven warming. Upstream precipitation exhibits a statistically significant positive relationship with T_{max} anomalies, although its regression coefficients are substantially smaller than those for Z500, indicating a secondary influence relative to large-scale circulation. However, our analysis framework cannot fully disentangle the effects of meridional sensible heat transport from latent heating associated with AR precipitation, suggesting that both mechanisms likely contribute to downstream warming.

Despite the dominant influence of Z500, AR orientation retains a statistically significant relationship with T_{max} anomalies during JJA at lag days 3–4. Importantly, this relationship persists after controlling for Z500, IVT, and precipitation anomalies, indicating that AR orientation contains information beyond simple differences in ridge amplitude or AR intensity. One possible explanation is that MARs preferentially transport heat and moisture poleward into the northeastern Pacific, altering the location and evolution of downstream ridging in ways that are not fully captured by regional-mean Z500 anomalies alone. The delayed emergence of the orientation signal several days after AR detection further suggests that AR geometry may influence the subsequent evolution of the large-scale circulation, rather than producing an immediate temperature response. In contrast, orientation effects in DJF are weaker and generally not statistically significant, implying that winter temperature anomalies are influenced by a broader range of processes, including cloud cover, precipitation, boundary-layer conditions, and transient synoptic disturbances. Together, these results support the conclusion that AR orientation provides additional predictive information regarding summertime warming in the PNW, while also reinforcing the central role of large-scale ridging in mediating AR-temperature relationships.

21698996, 2026, 16, Downloaded from https://agupubs.onlinelibrary.wiley.com/doi/10.1029/2026JD046646, Wiley Online Library on [11/11/2026]. See the Terms and Conditions (https://onlinelibrary.wiley.com/terms-and-conditions) on Wiley Online Library for rules of use; OA articles are governed by the applicable Creative Commons License

Finally, the timing of MAR-induced warming differs markedly from the evolution of the 2021 PNW heatwave. Although MARs generate substantial short-term warming across the PNW, the peak T_{max} anomalies in our composites occur two to three days after AR detection—well before the four-to-eight-day delay observed during the record-breaking 2021 heatwave (Figure 11). This temporal offset suggests that MARs can precondition the regional atmosphere through poleward heat and moisture advection but are insufficient alone to reproduce the extreme magnitude or persistence of that event. The subsequent amplification of the ridge, coupled with feedbacks from soil desiccation and prolonged subsidence (e.g., Li et al., 2024; Neal et al., 2022; Schumacher et al., 2022), likely extended and intensified the heatwave beyond typical MAR-driven responses. Consequently, the 2021 event exemplifies how AR-induced warming can serve as an initiating mechanism that, when combined with land–atmosphere and dynamical feedbacks, produces compounding extremes in the modern climate system.

5. Conclusions

Taken together, our results demonstrate that the thermal influence of atmospheric rivers on PNW surface temperatures depends critically on both their seasonal context and their geometric structure in the Northeast Pacific. Consistent with recent work showing that ARs can function as powerful agents of heat transport and surface warming (Gonzales et al., 2019; Scholz & Lora, 2024; Shields et al., 2019), we find that winter ARs with coherent meridional orientation reliably generate widespread positive T_{max} anomalies that persist for more than a week. In contrast, no consistent warming emerges from composite summer ARs unless they are first separated by orientation. Our classification of JJA ARs into meridionally tilted and zonally oriented events reveals a fundamental dynamical divide: MARs produce significant warming across the PNW, while ZARs induce cooling, reflecting the contrasting circulation patterns and associated thermal advection as well as differing cloud cover fraction. This geometric dependence explains why the AR preceding the 2021 heatwave—which tracked poleward into southwestern Canada—enhanced regional warming, yet also why ARs alone could not account for the event's unprecedented magnitude and duration. More broadly, our findings suggest that the orientation of an AR at a fixed offshore detection region provides meaningful information about its downstream thermal impact. This conclusion is further supported by the multiple linear regression analysis, which showed that AR orientation remains a significant predictor of JJA T_{max} anomalies at lag days 3–4 even after controlling for Z500, IVT, and precipitation anomalies. The persistence of this relationship suggests that AR geometry influences downstream temperature evolution through mechanisms not fully captured by ridge strength or AR intensity alone. In both seasonal composites and the broader climatology, knowing whether an approaching AR exhibits a meridional or zonal structure offers predictive value for anticipating the sign and strength of subsequent PNW temperature anomalies. As ARs intensify and become more thermodynamically potent under continued climate change (Gonzales et al., 2019), incorporating AR geometry into forecasting frameworks may improve early warnings for heat extremes in the PNW.

Acknowledgments
This research was supported by the Director, Office of Science, Office of Biological and Environmental Research of the U.S. Department of Energy under Contract No. DE-AC02-05CH11231 and by the Regional and Global Model Analysis Program area within the Earth and Environmental Systems Modeling Program. The research used resources of the National Energy Research Scientific Computing Center (NERSC), which is also supported by the Office of Science of the U.S. Department of Energy, under Contract No. DE-AC02-05CH11231. This research was supported in part by Lilly Endowment, Inc., through its support for the Indiana University Pervasive Technology Institute. This research was also supported in part by the Environmental Resilience Institute, funded by Indiana University's Prepared for Environmental Change Grand Challenge initiative.

Conflict of Interest

The authors declare no conflicts of interest relevant to this study.

Availability Statement

The ERA5 data can be obtained from Hersbach et al. (2020) and from the Climate Data Store website, https://cds.climate.copernicus.eu/. TECA-BARD (O'Brien et al., 2020) data can be created by using instructions from https://teca.readthedocs.io/en/latest/applications.html. Analysis code and figures are available at Goddard (2026).

References

Bartusek, S., Kornhuber, K., & Ting, M. (2022). 2021 North American heatwave amplified by climate change-driven nonlinear interactions. *Nature Climate Change*, *12*(12), 1143–1150. https://doi.org/10.1038/s41558-022-01520-4

Bercos-Hickey, E., O'Brien, T. A., Wehner, M. F., Zhang, L., Patricola, C. M., Huang, H., & Risser, M. D. (2022). Anthropogenic contributions to the 2021 Pacific Northwest heatwave. *Geophysical Research Letters*, *49*(23), e2022GL099396. https://doi.org/10.1029/2022GL099396

Domeisen, D. I. V., Eltahir, E. A. B., Fischer, E. M., Knutti, R., Perkins-Kirkpatrick, S. E., Schär, C., et al. (2022). Prediction and projection of heatwaves. *Nature Reviews Earth & Environment*, *4*(1), 36–50. https://doi.org/10.1038/s43017-022-00371-z

Duan, S. Q., McKinnon, K. A., & Simpson, I. R. (2025). The impact of soil preconditioning on the evolution of heatwaves under constrained circulation: A case study of the 2021 Pacific Northwest heatwave. *Earth's Future*, *13*(9), e2025EF006216. https://doi.org/10.1029/2025EF006216

Fleishman, E., Rupp, D. E., Loikith, P. C., Bumbaco, K. A., & O'neill, L. W. (2025). Synthesis of publications on the anomalous June 2021 heat wave in the Pacific Northwest of the United States and Canada. *Bulletin of the American Meteorological Society*, *106*(6), E1155–E1174. https://doi.org/10.1175/BAMS-D-24-0188.1

Goddard, P. B. (2026). Data and Code for Goddard et al 2026–PNW ARs and Tmax (1) [Computational Notebook & Dataset]. *Zenodo*. https://doi.org/10.5281/zenodo.18318314

Gonzales, K. R., Swain, D. L., Nardi, K. M., Barnes, E. A., & Diffenbaugh, N. S. (2019). Recent warming of landfalling atmospheric Rivers along the West Coast of the United States. *Journal of Geophysical Research: Atmospheres*, *124*(13), 6810–6826. https://doi.org/10.1029/2018JD029860

Guan, B., & Waliser, D. E. (2015). Detection of atmospheric rivers: Evaluation and application of an algorithm for global studies. *Journal of Geophysical Research: Atmospheres*, *120*(24), 12514–12535. https://doi.org/10.1002/2015JD024257

Heeter, K. J., Harley, G. L., Abatzoglou, J. T., Anchukaitis, K. J., Cook, E. R., Coulthard, B. L., et al. (2023). Unprecedented 21st century heat across the Pacific Northwest of North America. *npj Climate and Atmospheric Science*, *6*(1), 5. https://doi.org/10.1038/s41612-023-00340-3

Hersbach, H., Bell, B., Berrisford, P., Hirahara, S., Horányi, A., Muñoz-Sabater, J., et al. (2020). The ERA5 global reanalysis. *Quarterly Journal of the Royal Meteorological Society*, *146*(730), 1999–2049. https://doi.org/10.1002/QJ.3803

Li, X., Mann, M. E., Wehner, M. F., Rahmstorf, S., Petri, S., Christiansen, S., et al. (2024). Role of atmospheric resonance and land–atmosphere feedbacks as a precursor to the June 2021 Pacific Northwest heat dome event. *Proceedings of the National Academy of Sciences*, *121*(4), e2315330121. https://doi.org/10.1073/PNAS.2315330121

Lin, H., Mo, R., & Vitart, F. (2022). The 2021 Western North American heatwave and its subseasonal predictions. *Geophysical Research Letters*, *49*(6), e2021GL097036. https://doi.org/10.1029/2021GL097036

McKinnon, K. A., & Simpson, I. R. (2022). How unexpected was the 2021 Pacific Northwest heatwave? *Geophysical Research Letters*, *49*(18), e2022GL100380. https://doi.org/10.1029/2022GL100380

Miralles, D. G., Teuling, A. J., van Heerwaarden, C. C., & de Arellano, J. V. G. (2014). Mega-heatwave temperatures due to combined soil desiccation and atmospheric heat accumulation. *Nature Geoscience*, *7*(5), 345–349. https://doi.org/10.1038/ngeo2141

Mo, R., Lin, H., & Vitart, F. (2022). An anomalous warm-season trans-Pacific atmospheric river linked to the 2021 western North America heatwave. *Communications Earth & Environment 2022*, *3*(1), 1–12. https://doi.org/10.1038/s43247-022-00459-w

Neal, E., Huang, C. S. Y., & Nakamura, N. (2022). The 2021 Pacific Northwest heat wave and associated blocking: Meteorology and the role of an upstream cyclone as a diabatic source of wave activity. *Geophysical Research Letters*, *49*(8), e2021GL097699. https://doi.org/10.1029/2021GL097699

O'Brien, T. A., Risser, M. D., Loring, B., Elbashandy, A. A., Krishnan, H., Johnson, J., et al. (2020). Detection of atmospheric rivers with inline uncertainty quantification: TECA-BARD v1.0.1. *Geoscientific Model Development*, *13*(12), 6131–6148. https://doi.org/10.5194/GMD-13-6131-2020

Overland, J. E. (2021). Causes of the record-breaking Pacific Northwest heatwave, late June 2021. *Atmosphere*, *12*(11), 1434. https://doi.org/10.3390/ATMOS12111434

Papritz, L., & Röthlisberger, M. (2023). A novel temperature anomaly source diagnostic: Method and application to the 2021 heatwave in the Pacific Northwest. *Geophysical Research Letters*, *50*(23), e2023GL105641. https://doi.org/10.1029/2023GL105641

Philip, S. Y., Kew, S. F., van Oldenborgh, G. J., Anslow, F. S., Seneviratne, S. I., Vautard, R., et al. (2022). Rapid attribution analysis of the extraordinary heat wave on the Pacific coast of the US and Canada in June 2021. *Earth System Dynamics*, *13*(4), 1689–1713. https://doi.org/10.5194/ESD-13-1689-2022

Qian, Y., Hsu, P. C., Yuan, J., Zhu, Z., Wang, H., & Duan, M. (2022). Effects of subseasonal variation in the East Asian monsoon system on the summertime heat wave in Western North America in 2021. *Geophysical Research Letters*, *49*(8), e2021GL097659. https://doi.org/10.1029/2021GL097659

Scholz, S. R., & Lora, J. M. (2024). Atmospheric rivers cause warm winters and extreme heat events. *Nature*, *636*(8043), 640–646. https://doi.org/10.1038/s41586-024-08238-7

Schumacher, D. L., Hauser, M., & Seneviratne, S. I. (2022). Drivers and mechanisms of the 2021 Pacific Northwest heatwave. *Earth's Future*, *10*(12), e2022EF002967. https://doi.org/10.1029/2022EF002967

Shields, C. A., Rosenbloom, N., Bates, S., Hannay, C., Hu, A., Payne, A. E., et al. (2019). Meridional heat transport during atmospheric Rivers in high-resolution CESM climate projections. *Geophysical Research Letters*, *46*(24), 14702–14712. https://doi.org/10.1029/2019GL085565

Shields, C. A., Rutz, J. J., Leung, L. Y., Martin Ralph, F., Wehner, M., Kawzenuk, B., et al. (2018). Atmospheric River tracking method intercomparison project (ARTMIP): Project goals and experimental design. *Geoscientific Model Development*, *11*(6), 2455–2474. https://doi.org/10.5194/GMD-11-2455-2018

Terray, L. (2023). A storyline approach to the June 2021 Northwestern North American heatwave. *Geophysical Research Letters*, *50*(5), e2022GL101640. https://doi.org/10.1029/2022GL101640

White, R. H., Anderson, S., Booth, J. F., Braich, G., Draeger, C., Fei, C., et al. (2023). The unprecedented Pacific Northwest heatwave of June 2021. *Nature Communications 2023*, *14*(1), 1–20. https://doi.org/10.1038/s41467-023-36289-3

Zhang, X., Zhou, T., Zhang, W., Ren, L., Jiang, J., Hu, S., et al. (2023). Increased impact of heat domes on 2021-like heat extremes in North America under global warming. *Nature Communications*, *14*(1), 1–11. https://doi.org/10.1038/s41467-023-37309-y

21698996, 2026, 16, Downloaded from https://agupubs.onlinelibrary.wiley.com/doi/10.1029/2026JD046646, Wiley Online Library on [11/11/2026]. See the Terms and Conditions (https://onlinelibrary.wiley.com/terms-and-conditions) on Wiley Online Library for rules of use; OA articles are governed by the applicable Creative Commons License